

## Immobilization of Polymeric g-C<sub>3</sub>N<sub>4</sub> on Structured Ceramic Foam for Efficient Visible Light Photocatalytic Air Purification with Real Indoor Illumination

Fan Dong,<sup>\*,†</sup> Zhenyu Wang,<sup>†</sup> Yuhan Li,<sup>†</sup> Wing-Kei Ho,<sup>‡</sup> and S. C. Lee<sup>§</sup>

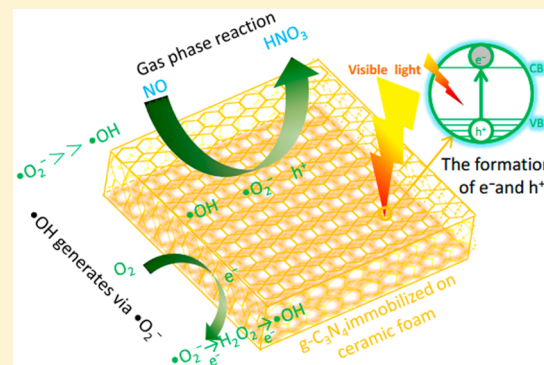
<sup>†</sup>Chongqing Key Laboratory of Catalysis and Functional Organic Molecules, College of Environmental and Biological Engineering, Chongqing Technology and Business University, Chongqing 400067, People's Republic of China

<sup>‡</sup>Department of Science and Environmental Studies, The Hong Kong Institute of Education, Tai Po, New Territories, Hong Kong, People's Republic of China

<sup>§</sup>Department of Civil and Environmental Engineering, The Hong Kong Polytechnic University, Hung Hom, Kowloon, Hong Kong, People's Republic of China

### Supporting Information

**ABSTRACT:** The immobilization of a photocatalyst on a proper support is pivotal for practical environmental applications. In this work, graphitic carbon nitride ( $\text{g-C}_3\text{N}_4$ ) as a rising visible light photocatalyst was first immobilized on structured  $\text{Al}_2\text{O}_3$  ceramic foam by a novel *in situ* approach. Immobilized  $\text{g-C}_3\text{N}_4$  was applied for photocatalytic removal of 600 ppb level NO in air under real indoor illumination of an energy-saving lamp. The photocatalytic activity of immobilized  $\text{g-C}_3\text{N}_4$  was gradually improved as the pyrolysis temperature was increased from 450 to 600 °C. The optimized conditions for  $\text{g-C}_3\text{N}_4$  immobilization on  $\text{Al}_2\text{O}_3$  supports can be achieved at 600 °C for 2 h. The NO removal ratio could reach up to 77.1%, exceeding that of other types of well-known immobilized photocatalysts. Immobilized  $\text{g-C}_3\text{N}_4$  was stable in activity and can be used repeatedly without deactivation. The immobilization of  $\text{g-C}_3\text{N}_4$  on  $\text{Al}_2\text{O}_3$  ceramic foam was found to be firm enough to overwhelm the continuous air flowing, which can be ascribed to the special chemical interaction between  $\text{g-C}_3\text{N}_4$  and  $\text{Al}_2\text{O}_3$ . On the basis of the 5,5'-dimethyl-1-pyrroline-N-oxide electron spin resonance (DMPO ESR) spin trapping and reaction intermediate monitoring, the active species produced from  $\text{g-C}_3\text{N}_4$  under illumination were confirmed and the reaction mechanism of photocatalytic NO oxidation by  $\text{g-C}_3\text{N}_4$  was revealed. The present work could provide new perspectives for promoting large-scale environmental applications of supported photocatalysts.



### 1. INTRODUCTION

Nitric oxide and nitrogen dioxide, jointly referred to as  $\text{NO}_x$ , are typical indoor and outdoor air pollutants with increasing environmental concern.<sup>1</sup>  $\text{NO}_x$  is one of the major contributors to acid rain and urban smog, which could trigger serious respiratory diseases, hospitalization for heart or lung diseases, and even premature death.<sup>2</sup> Various techniques have been developed for  $\text{NO}_x$  purification. The conventional approaches, such as selective catalytic reduction (SCR), wet scrubbing, adsorption, biofiltration, and catalytic decomposition, have been developed for  $\text{NO}_x$  removal.<sup>3–5</sup> However, they are not economically feasible for removal of air pollutants at a low concentration of the parts per billion (ppb) level, which is a typical concentration for indoor air quality.<sup>6,7</sup>

Visible light induced semiconductor photocatalysis as a green technology that could use natural sunlight or artificial indoor light to purify air pollutants of low concentration at ambient conditions, providing an attractive alternative to conventional approaches.<sup>8,9</sup> Several metal-containing visible light photo-

catalysts have been prepared and applied for enhanced removal of  $\text{NO}_x$  in air, such as doped  $\text{TiO}_2$ ,<sup>10,11</sup>  $\text{BiOX}$ ,<sup>12</sup>  $\text{Bi}_2\text{WO}_6$ ,<sup>13</sup>  $\text{BiVO}_4$ ,<sup>14</sup>  $\text{In}(\text{OH})_x\text{S}_y$ ,<sup>15</sup>  $\text{NiO}$ ,<sup>16</sup> N-doped  $(\text{BiO})_2(\text{CO}_3)_2$ ,<sup>17–19</sup> graphene/BiOBr nanocomposites,<sup>20</sup> and BiOI/BiOCl nanocomposites.<sup>21</sup> These photocatalysts are usually powdery without immobilization on a proper support.

Recently, polymeric graphitic carbon nitride ( $\text{g-C}_3\text{N}_4$ ) as a metal-free and sustainable visible light photocatalyst reported by Wang et al.<sup>22</sup> has attracted intensive interests because of its promising applications in solar energy conversion, environmental remediation, and selective organic synthesis.<sup>23–29</sup> Powdery  $\text{g-C}_3\text{N}_4$  has also been used in photocatalytic removal of  $\text{NO}_x$  in air and exhibited high activity.<sup>30,31</sup> However, the reaction mechanism of photocatalytic removal of  $\text{NO}_x$  with  $\text{g-C}_3\text{N}_4$  is still not clear.

Received: May 9, 2014

Revised: July 7, 2014

Accepted: August 8, 2014

Published: August 8, 2014

$\text{C}_3\text{N}_4$  is still unknown. For practical application, the operation mode of a powdery photocatalyst should employ technologically limited and time-consuming filtration processes to separate the nanosized powdery photocatalysts from the airflow. Without immobilization, the photocatalyst would be simply blown away and become lost. It is essential to develop a facile process to effectively immobilize the powdery  $\text{g-C}_3\text{N}_4$  photocatalyst on a proper support that could eliminate the costly phase separation process. To the best of knowledge, the immobilization of  $\text{g-C}_3\text{N}_4$  on the support for practical application has never been reported.

In this work, a novel *in situ* approach is developed for effective immobilization of  $\text{g-C}_3\text{N}_4$  on structured ceramic foam. The immobilization of  $\text{g-C}_3\text{N}_4$  on  $\text{Al}_2\text{O}_3$  ceramic foam was firm enough to overwhelm the continuous flowing air, owing to the special chemical interaction between  $\text{g-C}_3\text{N}_4$  and  $\text{Al}_2\text{O}_3$ . Furthermore, optimized supported  $\text{g-C}_3\text{N}_4$  showed an exceptionally high NO removal ratio of 77.1% under real indoor illumination of an energy-saving lamp. The reaction mechanism of photocatalytic removal of NO with  $\text{g-C}_3\text{N}_4$  was also revealed on the basis of 5,5'-dimethyl-1-pirroline-N-oxide electron spin resonance (DMPO ESR) spin trapping. The present investigation demonstrated that  $\text{g-C}_3\text{N}_4$  could be immobilized on  $\text{Al}_2\text{O}_3$  ceramic foam by a simple and economical process for efficient purification of NO in air under real indoor irradiation, which could promote the practical environmental application of an earth-abundant  $\text{g-C}_3\text{N}_4$  photocatalyst.

## 2. EXPERIMENTAL SECTION

**2.1. Immobilization of  $\text{g-C}_3\text{N}_4$  on Structured  $\text{Al}_2\text{O}_3$  Foam.** To immobilize a photocatalyst onto a support is essential for air purification.  $\text{g-C}_3\text{N}_4$  was immobilized on the  $\text{Al}_2\text{O}_3$  ceramic foam by an *in situ* thermal approach. In a typical process, 40 g of dicyandiamide powder and 300 mL of distilled water were put into the alumina crucible (160 × 160 × 78 mm) (see Figure S1a of the Supporting Information) and stirred for 15 min. The  $\text{Al}_2\text{O}_3$  ceramic foam (150 × 150 × 22 mm, 10 ppi) (see Figure S1b of the Supporting Information) was pretreated in a muffle furnace at 500 °C for 30 min and then immersed in the alumina crucible with dicyandiamide solution. Distilled water was then added to submerge the  $\text{Al}_2\text{O}_3$  ceramic foam. The crucible was transferred to an oven and dried at 80 °C for 10 h to recrystallize dicyandiamide. The crucible with a cover was put into a muffle furnace and then heated for 2 h at a certain temperature at a heating rate of 15 °C/min in static air. To investigate the effects of temperatures on the immobilization of  $\text{g-C}_3\text{N}_4$ , the temperatures were set at 450, 500, 550, and 600 °C, respectively. The resulting samples were labeled as CN-450, CN-500, CN-550, and CN-600, respectively. The typical visible light photocatalysts ( $\text{g-C}_3\text{N}_4$  derived from urea,  $\text{Bi}_2\text{WO}_6$ , and  $\text{BiOBr}$ ) were immobilized on  $\text{Al}_2\text{O}_3$  ceramic foam for comparison (see S1 of the Supporting Information for a detailed procedure).

**2.2. Characterization Methods and Active Species Analysis.** The crystal phase was analyzed by X-ray diffraction (XRD, model D/max RA, Japan) with Cu K $\alpha$  radiation at a scan rate of 0.01° 2 $\theta$ /s. X-ray photoelectron spectroscopy (XPS, Thermo ESCALAB 250, Waltham, MA) with Al K $\alpha$  X-ray radiation ( $h\nu = 1486.6$  eV) operated at 150 W was used to investigate the surface properties. Fourier transform infrared (FTIR) spectra were recorded on a Nicolet Nexus spectrometer on samples embedded in KBr pellets. Scanning electron microscopy (SEM, JEOL model JSM-6490, Japan) was

used to characterize the morphology of the samples. The morphologies and structures of the samples were examined by transmission electron microscopy (TEM, JEM-2010, Japan). The ultraviolet-visible (UV-vis) diffuse reflection spectra were obtained for the dry-pressed disk samples using a Scan UV-vis spectrophotometer [UV-vis diffuse reflectance spectroscopy (DRS), UV-2450, Shimadzu, Japan] equipped with an integrating sphere assembly using 100%  $\text{BaSO}_4$  as the reflectance sample. Nitrogen adsorption-desorption isotherms were obtained on a nitrogen adsorption apparatus (ASAP 2020, Micromeritics, Norcross, GA) with all samples degassed at 300 °C for 12 h prior to measurements. The photoluminescence spectra were measured with a fluorescence spectrophotometer (F-7000, Japan). The sample for ESR measurement (FLsp920, U.K.) was prepared by mixing  $\text{g-C}_3\text{N}_4$  in a 50 mM DMPO solution with aqueous dispersion for DMPO-•OH and methanol dispersion for DMPO-• $\text{O}_2^-$ . The visible light irradiation source was a 300 W Xe arc lamp (PLS-SXE 300, Beijing, China) system equipped with a UV cutoff filter ( $\lambda = 420$  nm).

### 2.3. Visible Light Photocatalytic Removal of NO in Air.

The photocatalytic activity was evaluated by removal of NO at ppb levels in a continuous flow reactor at the ambient temperature. The volume of the rectangular reactor, made of stainless steel and covered with Saint-Gobain Glass, was 4.5 L (30 × 15 × 10 cm). Two 13 W domestic energy-saving lamps (see Figure S1c of the Supporting Information) were placed outside the reactor vertically (see Figure S1d of the Supporting Information).  $\text{g-C}_3\text{N}_4$  immobilized on the foam was put into the reactor in the dark. NO gas was acquired from a compressed gas cylinder at a concentration of 100 ppm of NO ( $\text{N}_2$  balance). The initial concentration of NO was diluted to be 600 ppb by the air stream. The desired relative humidity (RH) level was controlled at 50% by passing the zero air streams through a humidification chamber. The gas streams were premixed completely by a gas blender, and the flow rate was controlled at 2.4 L/min by a mass flow controller. After the adsorption-desorption equilibrium was achieved, the lamp was turned on. The concentration of NO was continuously measured by a  $\text{NO}_x$  analyzer (Thermo Environmental Instruments, Inc., 42i-TL), which monitors NO and  $\text{NO}_2$  with a sampling rate of 1.0 L/min.  $\text{NO}_x$  in outlet steam was absorbed by the diluted NaOH aqueous solution. The removal ratio ( $\eta$ ) of NO was calculated as  $\eta (\%) = (1 - C/C_0) \times 100\%$ , where  $C$  and  $C_0$  are concentrations of NO in the outlet steam and feeding stream, respectively.

## 3. RESULTS AND DISCUSSION

### 3.1. Phase Structure and Chemical Composition.

Figure S2a of the Supporting Information shows the XRD patterns of  $\text{g-C}_3\text{N}_4$  loaded on  $\text{Al}_2\text{O}_3$  ceramic foam obtained under temperatures between 450 and 600 °C. All of the  $\text{g-C}_3\text{N}_4$  samples except for the CN-450 sample show similar diffraction patterns. The typical (002) interlayer stacking peak around 27.40° indicates the periodic graphitic stacking of the conjugated aromatic CN units with an interlayer distance of about 0.325 nm. Another minor diffraction peak around 13.0° can be assigned to the (100) plane corresponding to the void-void distance of the in-plane structural repeating motifs with a distance of about 0.681 nm.<sup>32,33</sup> At 450 °C, graphitic-like networks are formed but are incomplete because the reaction temperature is too low to complete the condensation of dicyandiamide.<sup>34</sup> The enlarged view of the (002) peak in Figure

S2b of the Supporting Information shows that the dominant peaks increase from  $27.17^\circ$  for CN-450 to  $27.73^\circ$  for CN-600. This result suggests that the interlayer distance of g-C<sub>3</sub>N<sub>4</sub> decreases when dicyandiamide is treated at higher temperatures. The diffraction peak intensity becomes stronger as the temperature is increased, indicating that the crystallinity of g-C<sub>3</sub>N<sub>4</sub> is improved correspondingly.<sup>35</sup>

The high-resolution XPS spectra of C 1s, N 1s, O 1s, Al 2p, Si 2p, and P 2p for CN-450 and CN-600 are shown in Figure S3 of the Supporting Information. The binding energies of C 1s at 284.6 and 288.1 eV can be ascribed to sp<sup>2</sup> C=C and C—N—C bonds from g-C<sub>3</sub>N<sub>4</sub>, respectively (see Figure S3a of the Supporting Information).<sup>36–38</sup> Two peaks at 398.7 and 400.3 eV of N 1s can be observed (see Figure S3b of the Supporting Information). The main peak centered at 398.7 eV originates from the sp<sup>2</sup>-bonded N involved in the triazine rings (C—N—C), and the weak peak at 400.3 eV is attributed to the tertiary nitrogen N—(C)<sub>3</sub> in g-C<sub>3</sub>N<sub>4</sub>.<sup>36–38</sup> Except for O and Al in the Al<sub>2</sub>O<sub>3</sub> foam (see panels c and d of Figure S3 of the Supporting Information), Si and P from the raw materials are detected (see panels e and f of Figure S3 of the Supporting Information). The XPS results suggest that g-C<sub>3</sub>N<sub>4</sub> is *in-situ*-immobilized on the surface of ceramic foam. The C/Al ratios of CN-450 and CN-600 are determined to be 8.7 and 14.6, indicating that the g-C<sub>3</sub>N<sub>4</sub> coverage of CN-600 on the support is higher than that of CN-450. Figure S3 of the Supporting Information shows that there are no significant differences in C 1s and N 1s regions. However, the peak intensity of O 1s, Al 2p, Si 2p, and P 2p for CN-600 is lower than that of CN-450 because the g-C<sub>3</sub>N<sub>4</sub> coverage in CN-600 is higher and the distribution of the g-C<sub>3</sub>N<sub>4</sub> layer on the support is more uniform (Figure 1), which is beneficial for photocatalytic activity enhancement. The FTIR spectra and their discussions can be found in Figure S4 of the Supporting Information.

**3.2. Microstructure and Formation Mechanism of g-C<sub>3</sub>N<sub>4</sub> Immobilizing on Al<sub>2</sub>O<sub>3</sub> Foam.** The microstructure of representative samples is investigated by SEM, as shown in Figure 1. Panels a and b of Figure 1 show the pristine porous Al<sub>2</sub>O<sub>3</sub> ceramic foam. The enlarged view in Figure 1c shows that the crystal particles are cumulated closely and macropores are formed in random distribution. Alumina ceramic foams as a superior photocatalytic support are made up of connected arrays of struts (panels c and d of Figure 1). This special design enables the processing of a high level of airflow at an ordinary pressure.<sup>39,40</sup> In addition, the surface/volume ratio is about 5–120 times greater than plates or other traditional supports with the same outer dimensions being offered.<sup>41</sup> In comparison to the traditional supports, the structure of ceramic foam could increase the use of light by multiple reflection of the light in the structure of cells and enhance the local light intensity. These advantages make the Al<sub>2</sub>O<sub>3</sub> ceramic foam an ideal support for immobilization of g-C<sub>3</sub>N<sub>4</sub>.

For sample CN-450, a layer of flaxen product is loaded on the support surface uniformly (panels e and f of Figure 1). Figure 1h shows that the layer that covered the surface of Al<sub>2</sub>O<sub>3</sub> foam gives rise to a blurry grain structure, while the number of macropores is decreased obviously. The enlarged view in Figure 1g shows that the surface of Al<sub>2</sub>O<sub>3</sub> ceramic foam is replaced by a continuous and rough layer structure. When the temperature is further increased to 600 °C, the particle surface of the support is covered uniformly by yellow g-C<sub>3</sub>N<sub>4</sub> (panels i and j of Figure 1). Moreover, the macropores on the surface of the Al<sub>2</sub>O<sub>3</sub> foam are filled by g-C<sub>3</sub>N<sub>4</sub> (Figure 1l). Further

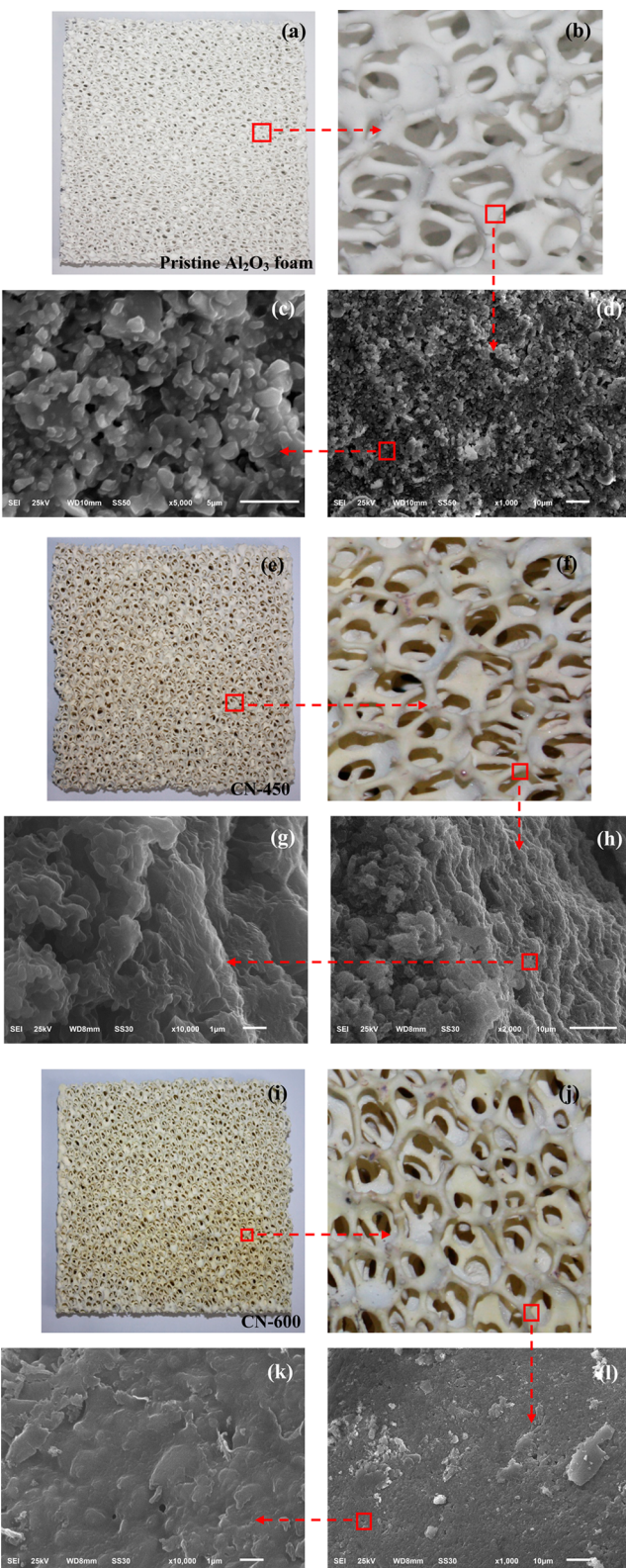


**Figure 1.** SEM images for (a–d) Al<sub>2</sub>O<sub>3</sub> foams, (e–h) CN-450, and (i–l) CN-600.

observation in Figure 1k indicates that the surface of the support is enveloped uniformly by g-C<sub>3</sub>N<sub>4</sub> layers and the surface is smooth. These results imply that the g-C<sub>3</sub>N<sub>4</sub> layers can be transformed into smaller nanoscale sheets, which are anchored closely on the cellular cells at higher temperatures. As

judged from the SEM observations, g-C<sub>3</sub>N<sub>4</sub> can be successfully immobilized on the surface of the Al<sub>2</sub>O<sub>3</sub> ceramic foam by a facile one-pot *in situ* approach.

The microstructure of g-C<sub>3</sub>N<sub>4</sub> samples peeled off from the support is further investigated by TEM, as shown in Figure S5 of the Supporting Information. The CN-500 sample is composed of large bulk particles with a layer structure (see panels a and b of Figure S5 of the Supporting Information). When the pyrolysis temperature is increased to 550 °C, the CN-550 sample is transformed into continuous thin layers with a smaller size because of the layers exfoliating and splitting (see panels c and d of Figure S5 of the Supporting Information).<sup>31</sup> When the temperature is further increased to 600 °C, the resulting CN-600 sample is transformed to thin, loose, and soft chip-like nanoarchitectures (see panels e and f of Figure S5 of the Supporting Information). The thickness of the layer is further reduced because of the layer splitting and exfoliation, which could increase the specific surface areas and porosity of g-C<sub>3</sub>N<sub>4</sub> layers (Table 1).<sup>25,31</sup>

**Table 1. S<sub>BET</sub> and Pore Volume of g-C<sub>3</sub>N<sub>4</sub> Samples Treated for Different Temperatures, NO Removal Ratio, and Weight of the Load of g-C<sub>3</sub>N<sub>4</sub> Samples**

sample name	S <sub>BET</sub> (m <sup>2</sup> /g)	pore volume (cm <sup>3</sup> /g)	$\eta_{(NO)}$ (%)	weight (g)
CN-450	5	0.15	60.0	20.103
CN-500	7	0.023	69.0	18.637
CN-550	26	0.097	72.3	17.166
CN-600	36	0.13	77.1	11.991

**3.3. Texture Property.** The nitrogen adsorption–desorption isotherms and Barrett–Joyner–Halenda (BJH) pore size distributions of g-C<sub>3</sub>N<sub>4</sub> samples peeled off from the support are displayed in Figure S6 of the Supporting Information. The adsorption–desorption isotherms (see Figure S6a of the Supporting Information) of the samples are of type IV [Brunauer, Deming, Deming, and Teller (BDDT) classification], suggesting the presence of mesopores (2–50 nm).<sup>42</sup> The hysteresis loops (see Figure S6b of the Supporting Information) are type H3 [International Union of Pure and Applied Chemistry (IUPAC) classification], which is associated with the slit-shaped pores resulting from the aggregates of plate-like particles (see Figure S5 of the Supporting Information). When the pyrolysis temperature is increased,

the hysteresis loops shift to the region of lower relative pressure and the areas of the hysteresis loops become large, indicating the formation of enlarged mesopores. The correlation among S<sub>BET</sub>, pore volume, and pyrolysis temperature are illustrated in Figure S7 and Table 1. Increasing the pyrolysis temperature from 500 to 600 °C results in a great enhancement of surface area and pore volume from 7 m<sup>2</sup>/g and 0.023 cm<sup>3</sup>/g for the CN-500 sample to 36 m<sup>2</sup>/g and 0.126 cm<sup>3</sup>/g for the CN-600 sample. The creation of the porous structure is associated with the reduced layer thickness and size (see Figure S5 of the Supporting Information). Figure S6b of the Supporting Information shows that the pore size distributions of g-C<sub>3</sub>N<sub>4</sub> samples are multimodal, where the smaller mesopores may reflect porosity within the nanoscale sheets and the larger mesopores are related to the pores formed between packed layers.

**3.4. Optical Properties and Band Gap.** Figure 2a shows the UV–vis DRS of the g-C<sub>3</sub>N<sub>4</sub> sample obtained under different temperatures. The absorption edges are varied by changing the temperature. When the pyrolysis temperature is increased from 450 to 600 °C, the absorption edges of g-C<sub>3</sub>N<sub>4</sub> are first red-shifted and then blue-shifted. The band gap values ( $E_g$ ) of g-C<sub>3</sub>N<sub>4</sub> samples are calculated by plots of  $(\alpha h\nu)^{1/2}$  versus photon energy, as shown in Figure 2b.<sup>33</sup> When the pyrolysis temperature increases from 450 to 550 °C, the band gap energy is decreased slightly from 2.70 to 2.61 eV. This bathochromic shift of the band gap can be explained by the structural change induced by the pyrolysis temperatures.<sup>43</sup> As the pyrolysis temperature was increased, the degree of polymerization became higher and the packing of the tri-s-triazine units became denser, leading to enhanced structural connections via enhanced van der Waals interaction between the tri-s-triazine cores. Such enhanced structural connections would result in a stronger overlap of the molecular orbital of the aromatic sheet stacks and, subsequently, alter the band gap of the g-C<sub>3</sub>N<sub>4</sub> sample.<sup>43</sup> When the pyrolysis temperature is further increased from 550 to 600 °C, the band gap energy is increased from 2.61 to 2.84 eV. This hypsochromic shift of the band gap is associated with the quantum confinement effect. The increased pyrolysis temperature could transform bulk g-C<sub>3</sub>N<sub>4</sub> into nanoscale sheets with reduced size and thickness, which could induce the quantum confinement effects, making the band gap of CN-600 enlarged.<sup>31,43</sup>

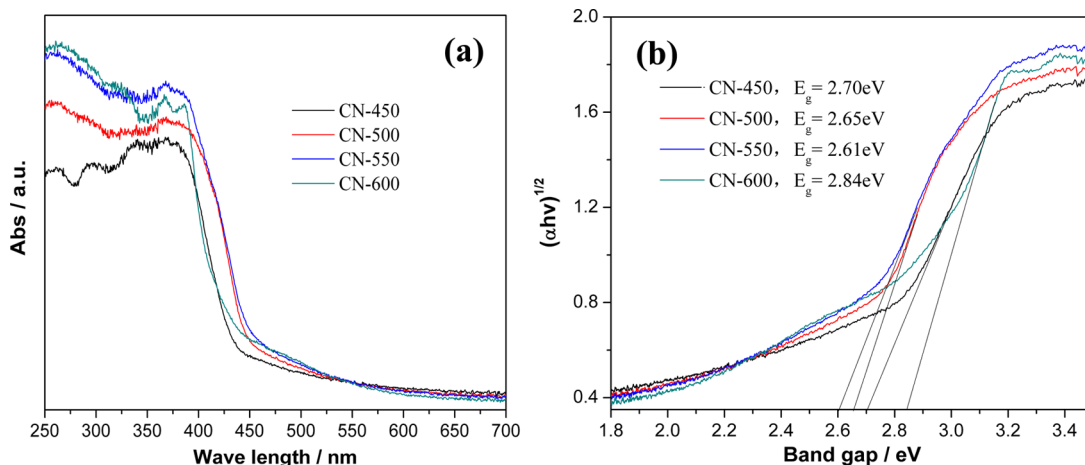


**Figure 2. (a)** UV–vis DRS and **(b)** plots of  $(\alpha h\nu)^{1/2}$  versus photon energy of g-C<sub>3</sub>N<sub>4</sub> samples treated for different temperatures.

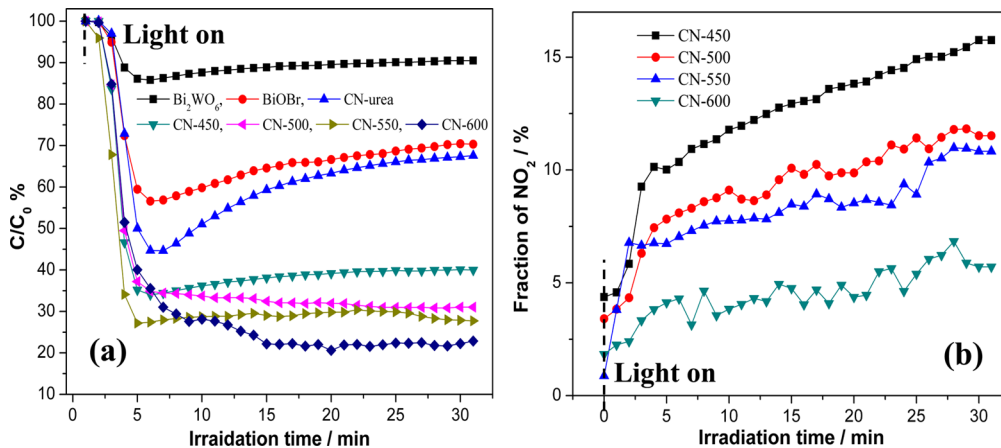


**Figure 3.** (a) Visible light photocatalytic activities of  $\text{g-C}_3\text{N}_4$  loaded on the  $\text{Al}_2\text{O}_3$  ceramic foam treated for different temperatures for removal of NO in air and (b) monitoring of  $\text{NO}_2$  intermediates during irradiation (continuous reactor, with a NO concentration of 600 ppb).

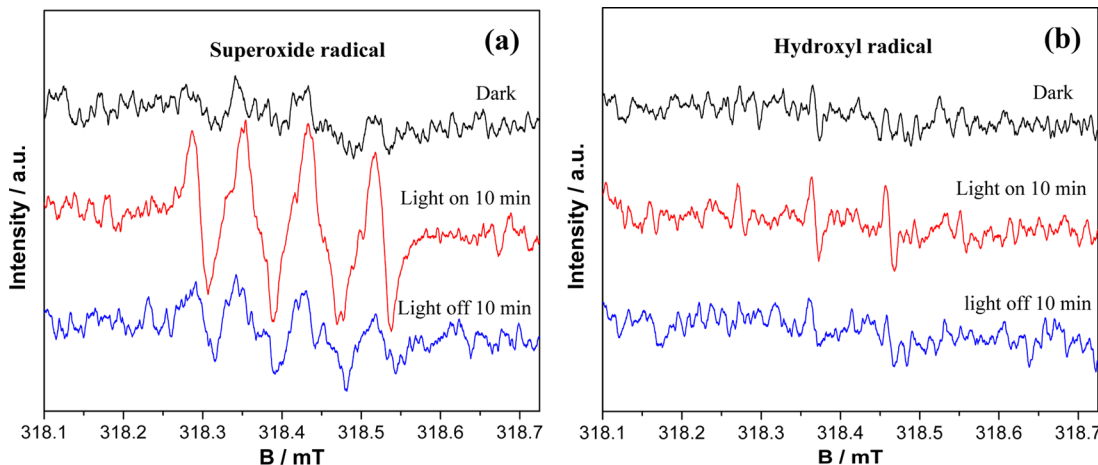


**Figure 4.** DMPO spin-trapping ESR spectra of CN-600 in (a) methanol dispersion for DMPO- $\cdot\text{O}_2^-$  and (b) aqueous dispersion for DMPO- $\cdot\text{OH}$ .

Figure S8 of the Supporting Information shows the room-temperature photoluminescence (PL) spectra of  $\text{g-C}_3\text{N}_4$  samples obtained under different temperatures. The PL peak position first shifts from 430 nm of the CN-450 sample to 455 nm of the CN-550 sample and then bathochromic shifts to 447 nm of the CN-600 sample, which is consistent with the band edge variation shown in Figure 2. The decreased PL intensity with an increasing temperature can be attributed to the enhanced charge separation, resulting from the enhanced crystallinity and reduced structural defects.<sup>44</sup> Because the PL emission originates from the recombination of electron–hole pairs, the decreased PL intensity indicates the enhanced charge carrier separation, which is favorable for improving the photocatalytic activity.

**3.5. Visible Light Photocatalytic Removal of NO and Reaction Mechanism.** Ceramic-foam-supported  $\text{g-C}_3\text{N}_4$  was employed for photocatalytic removal of NO in air under real indoor irradiation in a continuous mode to demonstrate their potential capability for air purification. The light source in Figure 3a shows the variation of the NO concentration ( $C/C_0$ , %) with irradiation time over  $\text{g-C}_3\text{N}_4$  loaded on the  $\text{Al}_2\text{O}_3$  foam treated under different temperatures. All samples exhibit respective visible light photocatalytic activity for NO removal.  $\text{g-C}_3\text{N}_4$  has a suitable band gap that can be excited directly by visible light. The removal of NO should be attributed to the reaction between NO and photogenerated radicals, producing a

final product of  $\text{HNO}_3$ .<sup>30,31</sup> For comparison,  $\text{g-C}_3\text{N}_4$  derived from urea (see Figure S9 of the Supporting Information),  $\text{Bi}_2\text{WO}_6$ , and  $\text{BiOBr}$  were loaded on  $\text{Al}_2\text{O}_3$  foam through simple impregnation methods.<sup>12,26,45</sup> When the pyrolysis temperature was increased from 450 to 600 °C, the mass of  $\text{g-C}_3\text{N}_4$  loaded on the foam was reduced from 20.103 g for CN-450 to 11.991 g for CN-600. The NO removal ratio over immobilized  $\text{g-C}_3\text{N}_4$  was increased from 60.0 to 77.1% with increasing pyrolysis temperatures. The CN-450 sample with high  $\text{g-C}_3\text{N}_4$  loading mass exhibits relatively low activity because the product on the foam is not pure in phase (see Figure S2 of the Supporting Information). When the temperature is increased to 600 °C, an unprecedented high activity of CN-600 can be achieved, which is more efficient than that of all of the reference samples. However, the pyrolysis temperature cannot be further elevated because  $\text{g-C}_3\text{N}_4$  will completely be decomposed when the temperature is higher than 650 °C. The high activity of CN-600 can be ascribed to the enhanced crystallinity (see Figure S2 of the Supporting Information), increased surface area and porosity (see Figure S6 of the Supporting Information), and promoted charge separation (see Figure S8 of the Supporting Information). First, the enhanced crystallinity is beneficial for reducing the structural defects and, thus, promoting the charge separation and transfer, as evidenced by PL (see Figure S8 of the Supporting Information). Second, the increased surface area

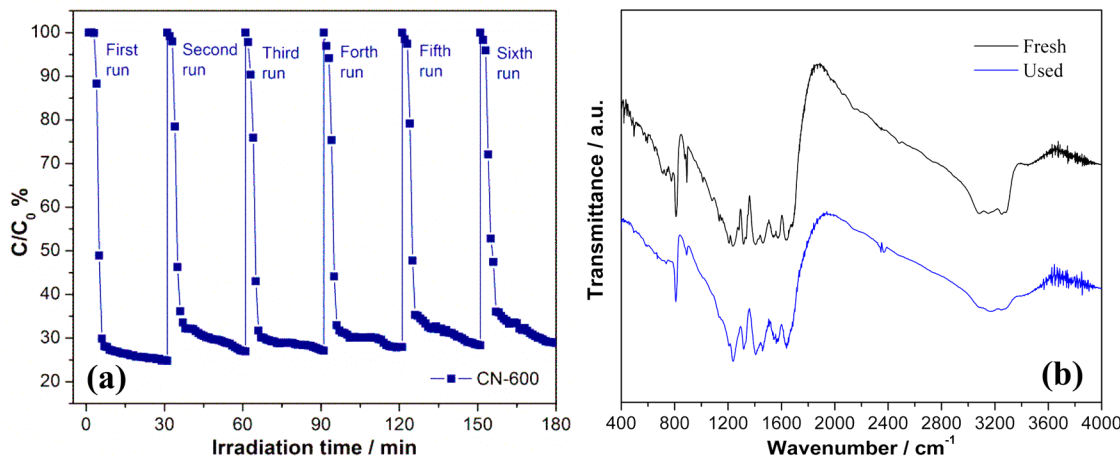
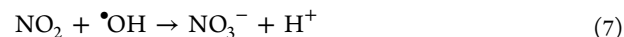
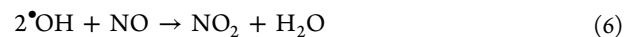
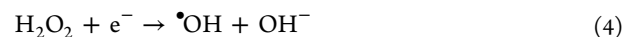
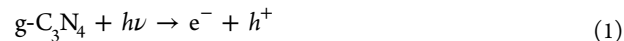


**Figure 5.** (a) Cycling runs for the photocatalytic degradation of NO over CN-600 under visible light irradiation and (b) FTIR spectra of CN-600 before and after cycling runs.

porosity could provide more active sites of the sample for photocatalysis and reactant diffusion.

The reaction intermediate of NO<sub>2</sub> during photocatalytic oxidation of NO is monitored as shown in Figure 3b. The percentage of the NO<sub>2</sub> concentration decreases with an increased pyrolysis temperature, which indicates that the oxidative capability of the CN-600 sample is stronger than other samples. This result is consistent with the enlarged band gap of CN-600 (Figure 2b) because the photoinduced charge carriers have increased redox potential, leading to enhanced oxidation ability.<sup>29</sup>

To verify the formation of reactive radicals accounting for the NO removal reaction, DMPO spin-trapping EPR measurements were employed for g-C<sub>3</sub>N<sub>4</sub> in methanol dispersion for DMPO-•O<sub>2</sub><sup>-</sup> (Figure 4a) and aqueous dispersion for DMPO-•OH (Figure 4b). Zhang et al. detected •O<sub>2</sub><sup>-</sup> and •OH over In(OH)<sub>x</sub>S<sub>y</sub> by DMPO spin-trapping EPR.<sup>15</sup> Under visible light illumination, the four strong characteristic peaks of the DMPO-•O<sub>2</sub><sup>-</sup> adduct can be clearly observed in Figure 4a, which demonstrates the massive production of -•O<sub>2</sub><sup>-</sup> via the reduction of O<sub>2</sub> with photogenerated electrons (eqs 1 and 2).<sup>15</sup> After staying in the dark for 10 min, the four peaks associated with DMPO-•O<sub>2</sub><sup>-</sup> adducts became depressed. In Figure 4b, the DMPO-•OH adduct signals were detected but the intensity of DMPO-•OH is significantly weaker than that of DMPO-•O<sub>2</sub><sup>-</sup>. Judging from the fact that the potential energy of valence band (VB) holes (1.40 eV) from g-C<sub>3</sub>N<sub>4</sub> is lower than that of OH<sup>-</sup>/•OH (1.99 eV) and H<sub>2</sub>O/•OH (2.37 eV), the holes cannot directly oxidize OH<sup>-</sup> or H<sub>2</sub>O into •OH. Alternatively, •OH should be generated via the transformation of •O<sub>2</sub><sup>-</sup> (eqs 3 and 4). Comparing the signal strength and the origination of the two radicals, we can conclude that •O<sub>2</sub><sup>-</sup> is the main reactive radical and •OH plays a minor role in the photocatalytic oxidation of NO (eqs 1–4). In addition, deducing from the electrode potential ( $E\phi$ ), the VB holes of g-C<sub>3</sub>N<sub>4</sub> sample might also oxidize NO because the  $E\phi_{VB}$  [about 1.4 eV versus normal hydrogen electrode (NHE)] of g-C<sub>3</sub>N<sub>4</sub> is more positive than  $E\phi$  (NO<sub>2</sub>/NO, 1.03 eV versus NHE),  $E\phi$  (HNO<sub>2</sub>/NO, 0.99 eV versus NHE), and  $E\phi$  (HNO<sub>3</sub>/NO, 0.94 eV vs NHE).<sup>15</sup> On the basis of these results, the reaction mechanism of photocatalytic removal of NO by g-C<sub>3</sub>N<sub>4</sub> is proposed, as shown in eqs 1–7.



**3.6. Photochemical Stability.** The stability and recyclability of photocatalysts are important for practical applications.<sup>10</sup> The cycling runs for the photocatalytic removal of NO with the CN-600 sample were performed. Figure 5a illustrates the relationship between the NO removal ratio and cycling times. After undergoing 6 repeated runs, the NO removal ratio still remains high, indicating that immobilized g-C<sub>3</sub>N<sub>4</sub> is stable in activity and can be used repeatedly. The CN-600 sample after cycling runs is collected and analyzed by FTIR (Figure 5b). It is obvious that the absorption band of the used CN-600 sample is identical to that of the fresh sample, which implies that the sample is stable in structure.

**3.7. Special Chemical Interaction between the Photocatalyst and Support.** The physicochemical interaction between g-C<sub>3</sub>N<sub>4</sub> and ceramic foam must be strong enough to overcome the continuous air flowing. The ideal photocatalyst support should have the following characteristics: (a) a strong binding force between the photocatalyst and the support without negatively affecting their activity, (b) the support not being decomposed under light irradiation, (c) chemically inert, (d) economically and technically realizable. The first essential requirement for a superior support is that the support–photocatalyst junction should resist strain derived from particle–particle and particle–airflow mechanical interactions to avoid the loss of catalyst particles from the support. The *in situ* immobilization approach as a novel method for supporting g-C<sub>3</sub>N<sub>4</sub> on alumina form is expected to satisfy the criteria above.

Whether g-C<sub>3</sub>N<sub>4</sub> can be firmly immobilized on the support is a central concern. We tested the firmness of g-C<sub>3</sub>N<sub>4</sub> loading

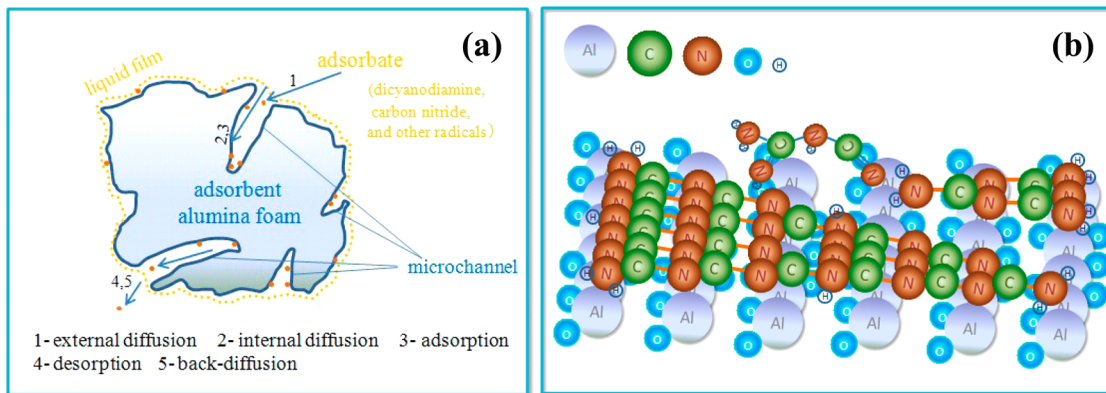


**Figure 6.** (a) Proposed mechanism of the physical adsorption process during the precursor dissolution–recrystallization process and (b) diagram of the bare Al atoms accepting an electron pair from g-C<sub>3</sub>N<sub>4</sub> and displaying L-acid property.

macroscopically by continuous air flowing (see Figure S10a of the Supporting Information). A fan is placed in front of the support immobilized with g-C<sub>3</sub>N<sub>4</sub> in a dark passage. The fan with strong air blowing works for more than 12 h consecutively. Later, the g-C<sub>3</sub>N<sub>4</sub> particles dropped from the supports were collected, and the weight was measured. It is found that the weight loss because of air flowing is below 0.15 g, which occupied less than 0.75% of g-C<sub>3</sub>N<sub>4</sub> immobilized on the alumina ceramic foam (see Figure S10b of the Supporting Information). The photoactive g-C<sub>3</sub>N<sub>4</sub> coating is just loose initially. This result indicates that g-C<sub>3</sub>N<sub>4</sub> could be immobilized on ceramic foam firmly, which could reduce the cost of catalyst replacement and recovery.

When the alumina foam is immersed in the dicyandiamide solution, a liquid thin film will form on the surface of the support through physical adsorption (Figure 6a). Dicyandiamide molecules could be anchored on both the external surface and internal surface, in which g-C<sub>3</sub>N<sub>4</sub> is generated by pyrolysis of dicyandiamide (see Figure S11 of the Supporting Information) and fills the pores of the support. The alumina surface shows mainly L-acid property, where the bare Al atoms in Al<sub>2</sub>O<sub>3</sub> could accept electron pairs (Figure 6b). The lone pairs of non-bonding electrons from the N atoms in g-C<sub>3</sub>N<sub>4</sub> could be accepted by bare Al atoms. As a result, a chemical binding force between g-C<sub>3</sub>N<sub>4</sub> and Al<sub>2</sub>O<sub>3</sub> foam is formed, which make the immobilization of g-C<sub>3</sub>N<sub>4</sub> on Al<sub>2</sub>O<sub>3</sub> extremely firm. This microscopic chemical interaction between the photocatalyst and support can be used to strengthen the g-C<sub>3</sub>N<sub>4</sub> immobilization. Thermogravimetry–differential scanning calorimetry (TG–DSC) was carried out to reveal the transformation process from pyrolysis of dicyandiamide (see Figure S12 of the Supporting Information and related discussion).

In summary, a novel *in situ* approach was developed for the immobilization of g-C<sub>3</sub>N<sub>4</sub> on structured Al<sub>2</sub>O<sub>3</sub> ceramic foam for air purification. Immobilized g-C<sub>3</sub>N<sub>4</sub> exhibited an unprecedented high and stable visible light photocatalytic performance toward removal of 600 ppb NO under indoor illumination. The efficient activity of CN-600 can be ascribed to the increased surface area and porosity, promoted charge separation, and enlarged band gap. The main reactive species responsible for g-C<sub>3</sub>N<sub>4</sub> photocatalysis were •O<sub>2</sub><sup>-</sup> radicals and photogenerated holes. The immobilization of g-C<sub>3</sub>N<sub>4</sub> on Al<sub>2</sub>O<sub>3</sub> ceramic foam was firm enough to overwhelm the continuous airflow because of the special chemical interaction. The present work could

greatly promote the large-scale environmental applications of Earth-abundant g-C<sub>3</sub>N<sub>4</sub> photocatalyst.

## ASSOCIATED CONTENT

### S Supporting Information

Experimental section for immobilization of reference photocatalysts, experimental setup for photocatalyst preparation and activity test (Figure S1), XRD pattern (Figure S2), XPS spectra (Figure S3), FTIR spectra (Figure S4), TEM images (Figure S5), N<sub>2</sub> adsorption–desorption isotherms and pore size distribution curves (Figure S6), correlation among S<sub>BET</sub>, pore volume, and pyrolysis temperature for g-C<sub>3</sub>N<sub>4</sub> samples (Figure S7), room temperature PL spectra (Figure S8), basic information on g-C<sub>3</sub>N<sub>4</sub> derived from urea (Figure S9), experimental setup of straight-blowing airflow simulation and the weight loss rate (Figure S10), diagram of g-C<sub>3</sub>N<sub>4</sub> synthesized by dicyanodiamine (Figure S11), and TG–DSC thermograms for heating dicyandiamide loaded on ceramic foam (Figure S12). This material is available free of charge via the Internet at <http://pubs.acs.org>.

## AUTHOR INFORMATION

### Corresponding Author

\*Telephone: +86-23-62769785-605. Fax: +86-23-62769785-605. E-mail: dfctbu@126.com.

### Notes

The authors declare no competing financial interest.

## ACKNOWLEDGMENTS

This research is financially supported by the National Natural Science Foundation of China (NSFC) (51108487), the Science and Technology Project from Chongqing (KJ1400617, cstc2013jcyjA20018 and cstc2013ykyfB50008), the Innovative Research Team Development Program in Chongqing (KJTD201314), the Innovative Project from Chongqing Technology and Business University (CTBU) (yjscxx2014-052-30), and the Early Career Scheme (ECS 809813) from the Research Grants Council (RGC) of Hong Kong.

## REFERENCES

- (1) Brickus, L. S.; Cardoso, J. N.; de Aquino Neto, F. R. Distributions of indoor and outdoor air pollutants in Rio de Janeiro, Brazil: Implications to indoor air quality in bayside offices. *Environ. Sci. Technol.* 1998, 32 (22), 3485–3490.

- (2) Su, C.; Ran, X.; Hu, J.; Shao, C. Photocatalytic process of simultaneous desulfurization and denitrification of flue gas by  $TiO_2$ –polyacrylonitrile nanofibers. *Environ. Sci. Technol.* **2013**, *47* (20), 11562–11568.
- (3) Heo, I.; Kim, M. K.; Sung, S.; Nam, I.-S.; Cho, B. K.; Olson, K. L.; Li, W. Combination of photocatalysis and HC/SCR for improved activity and durability of  $DeNO_x$  catalysts. *Environ. Sci. Technol.* **2013**, *47* (8), 3657–3664.
- (4) Guo, Q.; Sun, T.; Wang, Y.; He, Y.; Jia, J. Spray absorption and electrochemical reduction of nitrogen oxides from flue gas. *Environ. Sci. Technol.* **2013**, *47* (16), 9514–9522.
- (5) Epling, W. S.; Campbell, L. E.; Yezerets, A.; Currier, N. W.; Parks, J. E. Overview of the fundamental reactions and degradation mechanisms of  $NO_x$  storage/reduction catalysts. *Catal. Rev. Sci. Eng.* **2004**, *46* (2), 163–245.
- (6) Ai, Z.; Ho, W.; Lee, S.; Zhang, L. Efficient photocatalytic removal of NO in indoor air with hierarchical bismuth oxybromide nanoplate microspheres under visible light. *Environ. Sci. Technol.* **2009**, *43* (11), 4143–4150.
- (7) Huang, Y.; Ho, W.; Lee, S.; Zhang, L.; Li, G.; Yu, J. C. Effect of carbon doping on the mesoporous structure of nanocrystalline titanium dioxide and its solar-light-driven photocatalytic degradation of  $NO_x$ . *Langmuir* **2008**, *24* (7), 3510–3516.
- (8) Mo, J.; Zhang, Y.; Xu, Q.; Lamson, J. J.; Zhao, R. Photocatalytic purification of volatile organic compounds in indoor air: A literature review. *Atmos. Environ.* **2009**, *43* (14), 2229–2246.
- (9) Tong, H.; Ouyang, S.; Bi, Y.; Umezawa, N.; Oshikiri, M.; Ye, J. Nano-photocatalytic materials: Possibilities and challenges. *Adv. Mater.* **2012**, *24* (2), 229–251.
- (10) Ai, Z.; Zhu, L.; Lee, S.; Zhang, L. NO treated  $TiO_2$  as an efficient visible light photocatalyst for NO removal. *J. Hazard. Mater.* **2011**, *192* (1), 361–367.
- (11) Wu, X.; Yin, S.; Dong, Q.; Guo, C.; Kimura, T.; Matsushita, J.-i.; Sato, T. Photocatalytic properties of Nd and C codoped  $TiO_2$  with the whole range of visible light absorption. *J. Phys. Chem. C* **2013**, *117* (16), 8345–8352.
- (12) Zhang, W.; Zhang, Q.; Dong, F. Visible-light photocatalytic removal of NO in air over  $BiOX$  ( $X = Cl, Br, I$ ) single-crystal nanoplates prepared at room temperature. *Ind. Eng. Chem. Res.* **2013**, *52* (20), 6740–6746.
- (13) Li, G.; Zhang, D.; Yu, J. C.; Leung, M. K. An efficient bismuth tungstate visible-light-driven photocatalyst for breaking down nitric oxide. *Environ. Sci. Technol.* **2010**, *44* (11), 4276–4281.
- (14) Ai, Z.; Lee, S. Morphology-dependent photocatalytic removal of NO by hierarchical  $BiVO_4$  microboats and microspheres under visible light. *Appl. Surf. Sci.* **2013**, *280*, 354–359.
- (15) Ge, S.; Zhang, L. Efficient visible light driven photocatalytic removal of RhB and NO with low temperature synthesized  $In(OH)_xS_y$  hollow nanocubes: A comparative study. *Environ. Sci. Technol.* **2011**, *45* (7), 3027–3033.
- (16) Dong, Q.; Yin, S.; Guo, C.; Wu, X.; Kumada, N.; Takei, T.; Miura, A.; Yonesaki, Y.; Sato, T. Single-crystalline porous NiO nanosheets prepared from  $\beta-Ni(OH)_2$  nanosheets: Magnetic property and photocatalytic activity. *Appl. Catal., B* **2014**, *147*, 741–747.
- (17) Dong, F.; Ho, W.-K.; Lee, S.; Wu, Z.; Fu, M.; Zou, S.; Huang, Y. Template-free fabrication and growth mechanism of uniform  $(BiO)_2CO_3$  hierarchical hollow microspheres with outstanding photocatalytic activities under both UV and visible light irradiation. *J. Mater. Chem.* **2011**, *21* (33), 12428–12436.
- (18) Dong, F.; Sun, Y.; Ho, W.-K.; Wu, Z. Controlled synthesis, growth mechanism and highly efficient solar photocatalysis of nitrogen-doped bismuth subcarbonate hierarchical nanosheets architectures. *Dalton Trans.* **2012**, *41* (27), 8270–8284.
- (19) Dong, F.; Xiong, T.; Wang, R.; Sun, Y.; Jiang, Y. Growth mechanism and photocatalytic activity of self-organized N-doped  $(BiO)_2CO_3$  hierarchical nanosheets microspheres from bismuth citrate and urea. *Dalton Trans.* **2014**, *43* (18), 6631–6642.
- (20) Ai, Z.; Ho, W.; Lee, S. Efficient visible light photocatalytic removal of NO with  $BiOBr$ –graphene nanocomposites. *J. Phys. Chem. C* **2011**, *115* (51), 25330–25337.
- (21) Dong, F.; Sun, Y.; Fu, M.; Wu, Z.; Lee, S. Room temperature synthesis and highly enhanced visible light photocatalytic activity of porous  $BiOI/BiOCl$  composites nanoplates microflowers. *J. Hazard. Mater.* **2012**, *219*, 26–34.
- (22) Wang, X.; Maeda, K.; Thomas, A.; Takanabe, K.; Xin, G.; Carlsson, J. M.; Domen, K.; Antonietti, M. A metal-free polymeric photocatalyst for hydrogen production from water under visible light. *Nat. Mater.* **2009**, *8* (1), 76–80.
- (23) Wang, X.; Maeda, K.; Chen, X.; Takanabe, K.; Domen, K.; Hou, Y.; Fu, X.; Antonietti, M. Polymer semiconductors for artificial photosynthesis: Hydrogen evolution by mesoporous graphitic carbon nitride with visible light. *J. Am. Chem. Soc.* **2009**, *131* (5), 1680–1681.
- (24) Zhang, J.; Zhang, M.; Sun, R. Q.; Wang, X. A facile band alignment of polymeric carbon nitride semiconductors to construct isotype heterojunctions. *Angew. Chem., Int. Ed.* **2012**, *124* (40), 10292–10296.
- (25) Niu, P.; Zhang, L.; Liu, G.; Cheng, H. M. Graphene-like carbon nitride nanosheets for improved photocatalytic activities. *Adv. Funct. Mater.* **2012**, *22*, 4763–4770.
- (26) Dong, F.; Wang, Z.; Sun, Y.; Ho, W.-K.; Zhang, H. Engineering the nanoarchitecture and texture of polymeric carbon nitride semiconductor for enhanced visible light photocatalytic activity. *J. Colloid Interface Sci.* **2013**, *401*, 70–79.
- (27) Wang, Y.; Wang, X.; Antonietti, M. Polymeric graphitic carbon nitride as a heterogeneous organocatalyst: From photochemistry to multipurpose catalysis to sustainable chemistry. *Angew. Chem., Int. Ed.* **2012**, *51* (1), 68–89.
- (28) Zheng, Y.; Liu, J.; Liang, J.; Jaroniec, M.; Qiao, S. Z. Graphitic carbon nitride materials: Controllable synthesis and applications in fuel cells and photocatalysis. *Energy Environ. Sci.* **2012**, *5* (5), 6717–6731.
- (29) Wang, X.; Blechert, S.; Antonietti, M. Polymeric graphitic carbon nitride for heterogeneous photocatalysis. *ACS Catal.* **2012**, *2* (8), 1596–1606.
- (30) Dong, F.; Zhao, Z.; Xiong, T.; Ni, Z.; Zhang, W.; Sun, Y.; Ho, W.-K. In situ construction of  $g-C_3N_4/g-C_3N_4$  metal-free heterojunction for enhanced visible-light photocatalysis. *ACS Appl. Mater. Interfaces* **2013**, *5* (21), 11392–11401.
- (31) Dong, F.; Ou, M.; Jiang, Y.; Guo, S.; Wu, Z. Efficient and durable visible light photocatalytic performance of porous carbon nitride nanosheets for air purification. *Ind. Eng. Chem. Res.* **2014**, *53* (6), 2318–2330.
- (32) Bai, X.; Wang, L.; Zong, R.; Zhu, Y. Photocatalytic activity enhanced via  $g-C_3N_4$  nanoplates to nanorods. *J. Phys. Chem. C* **2013**, *117* (19), 9952–9961.
- (33) Dong, F.; Sun, Y.; Wu, L.; Fu, M.; Wu, Z. Facile transformation of low cost thiourea into nitrogen-rich graphitic carbon nitride nanocatalyst with high visible light photocatalytic performance. *Catal. Sci. Technol.* **2012**, *2* (7), 1332–1335.
- (34) Yan, S.; Li, Z.; Zou, Z. Photodegradation performance of  $g-C_3N_4$  fabricated by directly heating melamine. *Langmuir* **2009**, *25* (17), 10397–10401.
- (35) Dong, F.; Wu, L.; Sun, Y.; Fu, M.; Wu, Z.; Lee, S. Efficient synthesis of polymeric  $g-C_3N_4$  layered materials as novel efficient visible light driven photocatalysts. *J. Mater. Chem.* **2011**, *21* (39), 15171–15174.
- (36) Dong, F.; Li, Y.; Ho, W.; Zhang, H.; Fu, M.; Wu, Z. Synthesis of mesoporous polymeric carbon nitride exhibiting enhanced and durable visible light photocatalytic performance. *Chin. Sci. Bull.* **2014**, *59* (7), 688–698.
- (37) Zhang, J.; Zhang, G.; Chen, X.; Lin, S.; Möhlmann, L.; Dolega, G.; Lipner, G.; Antonietti, M.; Blechert, S.; Wang, X. Co-monomer control of carbon nitride semiconductors to optimize hydrogen evolution with visible light. *Angew. Chem., Int. Ed.* **2012**, *124* (13), 3237–3241.

- (38) Zhang, G.; Zhang, J.; Zhang, M.; Wang, X. Polycondensation of thiourea into carbon nitride semiconductors as visible light photocatalysts. *J. Mater. Chem.* **2012**, *22* (16), 8083–8091.
- (39) Yao, Y.; Ochiai, T.; Ishiguro, H.; Nakano, R.; Kubota, Y. Antibacterial performance of a novel photocatalytic-coated cordierite foam for use in air cleaners. *Appl. Catal., B* **2011**, *106* (3), 592–599.
- (40) Kouamé, A. N.; Masson, R.; Robert, D.; Keller, N.; Keller, V.  $\beta$ -SiC foams as a promising structured photocatalytic support for water and air detoxification. *Catal. Today* **2013**, *209*, 13–20.
- (41) Lin, H.; Valsaraj, K. T. Development of an optical fiber monolith reactor for photocatalytic wastewater treatment. *J. Appl. Electrochem.* **2005**, *35* (7–8), 699–708.
- (42) Pierotti, R.; Rouquerol, J. Reporting physisorption data for gas/solid systems with special reference to the determination of surface area and porosity. *Pure Appl. Chem.* **1985**, *57* (4), 603–619.
- (43) Zhang, G.; Zhang, J.; Zhang, M.; Wang, X. Polycondensation of thiourea into carbon nitride semiconductors as visible light photocatalysts. *J. Mater. Chem.* **2012**, *22* (16), 8083–8091.
- (44) Chen, X.; Zhang, J.; Fu, X.; Antonietti, M.; Wang, X. Fe-g-C<sub>3</sub>N<sub>4</sub>-Catalyzed oxidation of benzene to phenol using hydrogen peroxide and visible light. *J. Am. Chem. Soc.* **2009**, *131* (33), 11658–11659.
- (45) Tang, J.; Zou, Z.; Ye, J. Photocatalytic decomposition of organic contaminants by Bi<sub>2</sub>WO<sub>6</sub> under visible light irradiation. *Catal. Lett.* **2004**, *92* (1–2), 53–56.